Draft version January 16, 2019
Typeset using LaTeX **twocolumn** style in AASTeX62

That's No Moon: New Analysis Shows No Evidence for Lunar Companion Orbiting Kepler-1625b

Laura Kreidberg,[1,2] Rodrigo Luger, and Megan Bedell

[1] *Harvard Society of Fellows, 78 Mount Auburn Street, Cambridge, MA 02138*
[2] *Harvard-Smithsonian Center for Astrophysics, 60 Garden Street, Cambridge, MA 02138*

Submitted to AJ

ABSTRACT

The planet Kepler-1625b was recently suggested to have an EXOMOON. We present here a reanalysis of the *HST*/WFC3 observations of the Kepler-1625 system. We find that the data are well fit with a single transit model. We also do a moon model, and it is not favored. Upper limit on moon. Instrument systematics? Focus searches for exomoons on alternative targets.

Keywords: planets and satellites: individual (Kepler-1625b)

1. INTRODUCTION

Moons are abundant in the Solar System, and provide clues to the formation history, evolution, and even habitability of the planets they orbit. The great scientific potential of moons has prompted extensive search for lunar companions in exoplanetary systems (exomoons), and creative development of new search techniques (e.g. Kipping 2009a,b; Kipping et al. 2013; Simon et al. 2010; Peters & Turner 2013; Heller et al. 2014; Noyola et al. 2014; Hippke 2015; Agol et al. 2015; Sengupta & Marley 2016; Vanderburg et al. 2018).

Recently, a potential exomoon candidate was identified in the Kepler-1625 system (Teachey et al. 2018). The host planet, Kepler-1625b, is fairly long-period large world, with a radius consistent with that of Jupiter and an orbital period of 287 days. long period makes it ideal for stability of moon!

It was discovered in the Analysis of the four-year *Kepler* mission (Teachey & Kipping 2018).

Of the FIXME transits observed by *Kepler* FIXME what did they show.

Recently, analysis by FIXME of *Kepler* observations of FIXME suggested a moon. Follow-up happened.

(**?**) found moon was model dependent

2. OBSERVATIONS AND DATA REDUCTION

The Kepler-1625 system was observed with 26 continuous *HST* orbits on 28 - 29 October, 2017 (Program GO 15149: PI: A. Teachey). The observations used the Wide Field Camera 3 (WFC3) G141 grism in staring mode, which fixed the spectrum in a constant position on the detector. At the beginning of the visit, there was a single exposure taken with the F130N filter, which is used to determine the position of the spectral trace. The following exposures used the G141 grism with the `SPARS25`, `NSAMP`=15 readout pattern (exposure time of 290.8 seconds; 9 exposures per orbit). For additional description of the observation design, see Teachey & Kipping (2018).

We reduced the *HST* data using custom software developed in Kreidberg et al. (2014). This software has yielded consistent results with multiple independent pipelines (e.g. Knutson et al. 2014; Spake et al. 2018). We ran our pipeline on the `flt` data product provided by the Space Telescope Science Institute (STScI). The `flt` files are corrected for dark current, bias, and nonlinearity, and they are cleaned of cosmic ray hits based on a fit to the up-the-ramp samples. In keeping with previous WFC3 analysis, we discarded the first orbit of data, where the instrument systematics have larger amplitude. We also discard exposures taken during the South Atlantic Anomaly passage (exposures 107, 116, 125, and 126).

To begin the data reduction, we fit the centroid of the direct image with a two-dimensional Gaussian. The centroid position determines the position of the spectral trace, which we calculated using the coeffients provided in the configuration file from STScI: `G141.F130N.V4.32.conf`[1]. To process the spectra, we flatfielded the raw data using the spectroscopic flatfield coefficients provided by STScI in `WFC3.IR.G141.flat.2.fits`, following the instructions

[1] available at http://www.stsci.edu/hst/wfc3/analysis/grism_obs/calibrations/wfc3_g141.html

in Section 6 of the aXe User Manual[2]. We then created an extraction box centered on the spectral trace. We varied the height and width of the box in 1-pixel increments to find the window that minimized the root-mean-square (rms) deviation from the best fit to the transit light curve. The best was FIXME .

We reduced the grism exposures with the optimal extraction routine of Horne (1986), which minimizes background noise in the extracted spectrum by weighting pixels that are dominated by the target spectrum more heavily than pixels dominated by the background. The inputs for optimal extraction are the background-subtracted data array, the error array (including photon noise read noise, and uncertainty due to background subtraction), an initial guess for the spectrum and its uncertainty, and a mask array for bad pixels. For the initial guess of the spectrum and its uncertainty, we did a simple box extraction (sum over all rows in the extraction window), and assumed the variance was equal to the box-extracted spectrum (expected for photon noise limit). We measured and subtracted the background from the data array as described in 2.1. For the error array, we used a quadrature sum of the photon noise (the square root of the pixel counts), the read noise (12 photoelectrons for `flt` files; WFC3 Data Handbook[3]), and the error due to background subtraction (described in 2.1). The initial bad pixel mask included pixels marked with the data quality flag 4 or 512 (dead pixels or blobs).

In brief, optimal extraction is an iterative procedure with the following steps. First, we created a smoothed image by median-filtering each row of the data with a 9-pixel-wide window. We then normalized the smoothed image by dividing each column by its sum, and multiplied it by the best guess spectrum. We compared the smoothed image to the real data and masked outliers in the data that are greater than a threshold $\sigma_{\rm cut}$. We then recomputed the best guess spectrum with the new mask and the optimal weights from Horne (1986). The process is iterated until no outliers greater than the threshold remain. This procedure masks any cosmic rays or bad pixels that were missed by the initial `flt` calibration. We tested a range of thresholds ($4 < \sigma_{\rm cut} < 15$) and found that different $\sigma_{\rm cut}$ choices did not significantly change the final transit light curve. The data reported in this work use $\sigma_{\rm cut} = 15$. To create the braodband transit light curve, we sum each spectrum over all wavelengths.

[2] http://axe-info.stsci.edu/

[3] http://www.stsci.edu/hst/wfc3/documents/handbooks/currentDHB/

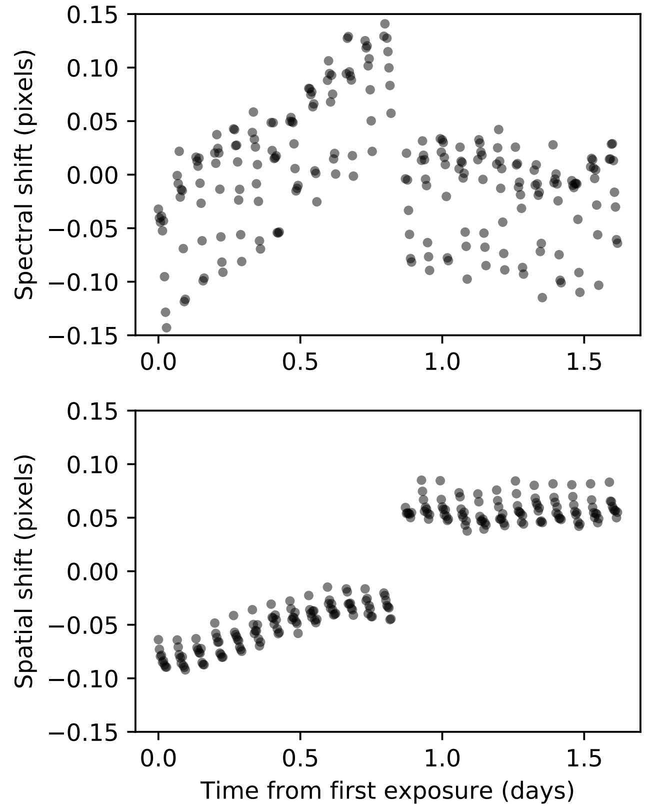

Figure 1. Shift (in pixels) relative to the mean position of the spectrum in the spectral direction (top) and spatial direction (bottom). The largest shift occurs after orbit 14 due to a guide star reacquisition.

2.1. *Background Subtraction*

The star Kepler-1625 is faint (H mag = 14.0) relative to most other exoplanet host stars observed with WFC3, which makes accurate background subtraction especially important for this target. Moreover, the host star is in a crowded field, so the pixels used to estimate the background must be chosen carefully to avoid contamination from other stars. We identified several uncontaminated regions by eye: $130 < X < 215$ and $6 < Y < 24$; $220 < X < 250$ and $110 < X < 155$; $6 < X < 47$ and $127 < Y < 141$, where X and Y are pixel numbers in the spectral and spatial direction, respectively (numbering from zero). To estimate the background and its uncertainty for each exposure, we took the median and median absolute deviation (MAD) of the pixel counts in these three regions. The per pixel uncertainty due to background subtraction is 1.4826 times the MAD.

2.2. *Pointing Drift Measurement*

The position of the spectrum on the detector shifts slightly over time (~ 0.1 pixel/day) due to the spacecraft's pointing drift. This drift can change the flux measured for the target star: if the spectrum moves onto less sensitive pixels, fewer photoelectrons are recorded. To enable a correction for this effect, we measured the position of the spectrum over time.

To measure shifts in the spatial direction, we first summed each `flt` image over all columns (which we dub the "column sum"). We used the first exposure in the visit as a template, and for each subsequent exposure, we used least-squares minimization to calculate the shift in pixels that minimized the difference between its column sum and the template. The shifts are a fraction of a pixel, so we used the NumPy `interp` routine to do linear interpolation on a sub-pixel scale. The WFC3 point spread function is undersampled, so we convolved each column sum with a 4-pixel-wide Gaussian before the interpolation (following Deming et al. 2013).

To measure the spectral shifts, we repeated this procedure with two differences: (1) we used the optimally extracted spectrum rather than the column sum; and (2) in addition to calculating the best fit shift, we also calculated a best fit normalization factor (a scalar multiple for the whole spectrum), to ensure that our results are not biased by the varying brightness of the host star during the planet's transit.

Figure 1 shows the best fit shifts. Over the entire 26-orbit visit, the maximum shift is less than 0.2 pixel in the spatial direction and 0.3 pixel in the spectral direction. The largest shift occurs after orbit 14, when the telescope reacquired the guide stars.

3. ANALYSIS

The raw light transit light curve (shown in Figure ??) contains both astrophysical signal and instrument systematic noise, which we model simultaneously.

3.1. *Astrophysics Model*

For the astrophysics, we used the `planetplanet` package (?), a photodynamical code that calculates light curves for multiple occulting bodies orbiting a star. Within `planetplanet`, the orbits are computed with the N-body integrator `REBOUND` (?). In our analysis, we considered two scenarios: a no-moon model and a moon model. The free parameters for the no-moon model were: the stellar radius R_*, the planet radius $R_{\rm planet}$, the time of central transit $t_{\rm planet}$, and the planet inclination i. For the moon model, we added a third body with radius $R_{\rm moon}$, transit time $t_{\rm moon}$, and orbital period $P_{\rm moon}$. We fixed the inclination of the moon to 90° to exclude grazing transit scenarios, where the moon radius could be arbitrarily large. We also fixed the moon mass and eccentricity to zero. We fixed the planet's orbital period to 287.378949 days (Teachey & Kipping 2018). For both the moon and no-mooon models, we fixed the planet eccentricity to zero and the mass to $1\,M_{\rm Jup}$. The `planetplanet` model uses these input parameters and returns the relative system flux for each exposure.

3.1.1. *Stellar Parameters*

For both the moon and no-moon scenarios, we used a quadratic stellar limb darkening law and fixed the coefficients to the prediction for a 5700 K, solar metallicity `PHOENIX` model from Espinoza & Jordán (2015); $u_1, u_2 = [0.216, 0.183]$.

We estimated the host star parameters using the Gaia DR2 parallax (Gaia Collaboration et al. 2016, 2018) along with UBV photometry from Everett et al. (2012) and JHK photometry from 2MASS (Skrutskie et al. 2006). We employed the isochrone python package (?) with the Dartmouth isochrone grid (Dotter et al. 2008) to obtain posterior constraints on the stellar parameters. The resulting parameters indicate that Kepler-1625 has stellar mass $1.37^{+0.13}_{-0.16}$ M$_\odot$, radius $1.81^{+0.18}_{-0.16}$ R$_\odot$, and age $2.8^{+1.6}_{-1.2}$ Gyr. In our analysis, we fixed the stellar mass to the best fit value ($1.37\,M_\odot$), and used a Gaussian prior on the radius, $R_* \sim N(1.81, 0.17)$.

3.2. *Instrument Systematics Model*

There are two systematic trends in the data. One is the orbit-long ramp, attributed to charge traps in the detector filling up over the orbit (Zhou et al. 2017). The other is a visit-long trend over multiple orbits, which could be due to shifts in the target star position onto more/less sensitive pixels.

To fit the orbit-long ramp, we used the non-parametric model from Teachey & Kipping (2018), which assigns each of the nine exposures per orbit a normalization constant, $c_1, ..., c_9$. To fit the visit-long trend, we used a linear combination of X and Y position (the shift relative to the mean in the spatial and spectral directions, respectively; shown in Figure 1). In sum, for exposure number i, the systematics model is:

$$S_i = c_j \times (1 + aX_i + bY_i) \tag{1}$$

where a and b, and c_j are free parameters, and $j = i \bmod 9 + 1$ is the exposure number relative to the first exposure in the orbit.

We also considered a second, more complex systematics model, S_2, which added a visit-long quadratic trend. A long-term trend was favored by the Teachey & Kipping (2018) analysis, and has been observed in other long-duration WFC3 time series (e.g. Stevenson et al. 2014; Kreidberg et al. 2018). The model is:

$$S_{2,i} = c_j \times (1 + aX_i + bY_i) \times (1 + vt_i + v_2 t_i^2) \tag{2}$$

where v and v_2 are free parameters and t_i is the time elapsed since the first exposure in the visit.

3.3. *Light Curve Fits*

We fit the raw, broadband transit light curve using the models described above. For comparison, we also fit the raw light curve from Teachey & Kipping (2018). In total, we fit each data set with four different models:

1. No moon, non-parametric ramp, X-Y decorrelation
2. Moon, non-parametric ramp, X-Y decorrelation
3. No moon, non-parametric ramp, X-Y decorrelation, visit-long polynomial
4. Moon, non-parametric ramp, X-Y decorrelation, visit-long polynomial

For each model, we determined the best fit parameters with least-squares minimization. We also ran a Markov chain Monte Carlo (MCMC) fit to determine the posterior probability of each parameters. The MCMC used the `emcee` package (Foreman-Mackey et al. 2013) with 50 walkers and ran for 10^4 steps.

4. RESULTS

Figure FIXME shows the best fits.

5. DISCUSSION

We did not find evidence for the exomoon. Why are we different from Teachey and Kipping?

Alex Teachey, Dan Foreman-Mackey

The HST data presented in this paper were obtained from the Mikulski Archive for Space Telescopes (MAST). STScI is operated by the Association of Universities for Research in Astronomy, Inc., under NASA contract NAS5-26555. Support for MAST for non-HST data is provided by the NASA Office of Space Science via grant NNX13AC07G and by other grants and contracts. We also use data from the European Space Agency (ESA) mission *Gaia* (https://www.cosmos.esa.int/gaia), processed by the *Gaia* Data Processing and Analysis Consortium (DPAC, https://www.cosmos.esa.int/web/gaia/dpac/consortium). Funding for the DPAC has been provided by national institutions, in particular the institutions participating in the *Gaia* Multilateral Agreement. We also use data products from the Two Micron All Sky Survey, which is a joint project of the University of Massachusetts and the Infrared Processing and Analysis Center/California Institute of Technology, funded by the National Aeronautics and Space Administration and the National Science Foundation. This research has made use of the SIMBAD database, operated at CDS, Strasbourg, France; the REBOUND integrator package (**?**); the NumPy package (Van Der Walt et al. 2011); and NASA's Astrophysics Data System.

REFERENCES

Agol, E., Jansen, T., Lacy, B., Robinson, T. D., & Meadows, V. 2015, ApJ, 812, 5, doi: 10.1088/0004-637X/812/1/5

Deming, D., Wilkins, A., McCullough, P., et al. 2013, ApJ, 774, 95, doi: 10.1088/0004-637X/774/2/95

Dotter, A., Chaboyer, B., Jevremović, D., et al. 2008, ApJS, 178, 89, doi: 10.1086/589654

Espinoza, N., & Jordán, A. 2015, MNRAS, 450, 1879, doi: 10.1093/mnras/stv744

Everett, M. E., Howell, S. B., & Kinemuchi, K. 2012, Publications of the Astronomical Society of the Pacific, 124, 316, doi: 10.1086/665529

Foreman-Mackey, D., Hogg, D. W., Lang, D., & Goodman, J. 2013, PASP, 125, 306, doi: 10.1086/670067

Gaia Collaboration, Prusti, T., de Bruijne, J. H. J., et al. 2016, A&A, 595, A1, doi: 10.1051/0004-6361/201629272

Gaia Collaboration, Brown, A. G. A., Vallenari, A., et al. 2018, A&A, 616, A1, doi: 10.1051/0004-6361/201833051

Heller, R., Williams, D., Kipping, D., et al. 2014, Astrobiology, 14, 798, doi: 10.1089/ast.2014.1147

Hippke, M. 2015, ApJ, 806, 51, doi: 10.1088/0004-637X/806/1/51

Horne, K. 1986, PASP, 98, 609, doi: 10.1086/131801

Kipping, D. M. 2009a, MNRAS, 392, 181, doi: 10.1111/j.1365-2966.2008.13999.x

—. 2009b, MNRAS, 396, 1797, doi: 10.1111/j.1365-2966.2009.14869.x

Kipping, D. M., Hartman, J., Buchhave, L. A., et al. 2013, ApJ, 770, 101, doi: 10.1088/0004-637X/770/2/101

Knutson, H. A., Dragomir, D., Kreidberg, L., et al. 2014, ApJ, 794, 155, doi: 10.1088/0004-637X/794/2/155

Kreidberg, L., Bean, J. L., Désert, J.-M., et al. 2014, Nature, 505, 69, doi: 10.1038/nature12888

Kreidberg, L., Line, M. R., Parmentier, V., et al. 2018, AJ, 156, 17, doi: 10.3847/1538-3881/aac3df

Noyola, J. P., Satyal, S., & Musielak, Z. E. 2014, ApJ, 791, 25, doi: 10.1088/0004-637X/791/1/25

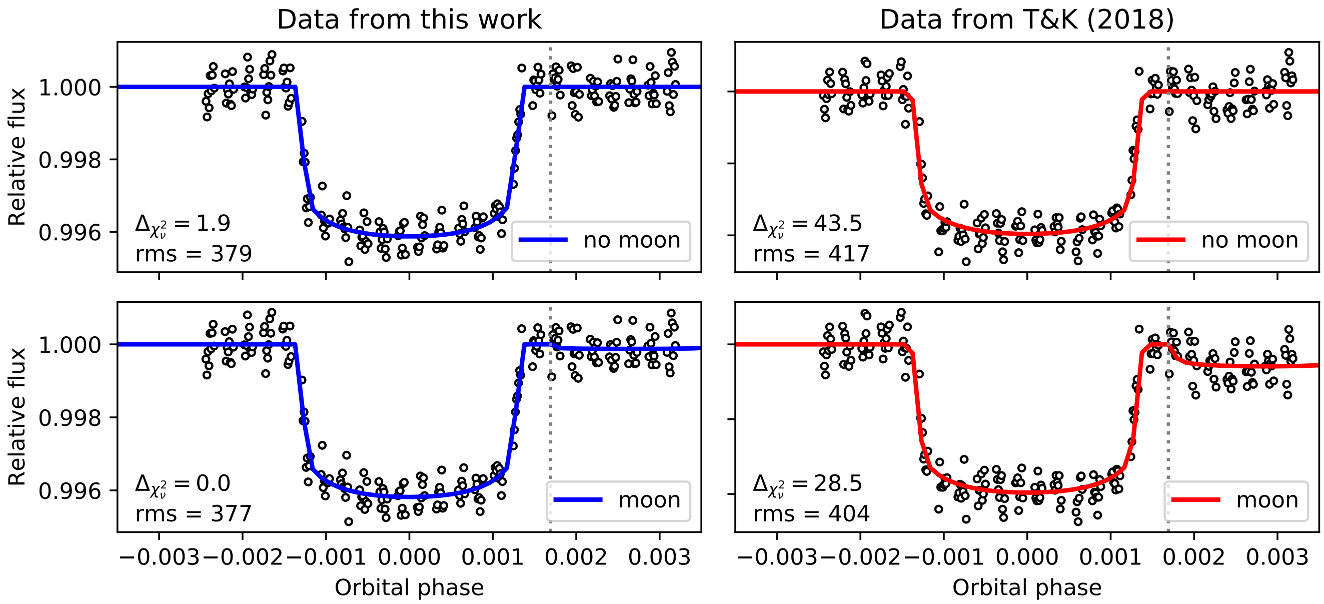

Figure 2. Best fit models compared to transit light curves from this work (left) and from TK18 (right). The top panel shows the best fit no-moon model (blue), and the bottom shows the best fit moon model (red). The lower left of each panel indicates the fit rms (in ppm) and the Δ_{χ_2} relative to the overall best fit (data reduction from this work, moon model). The dotted gray line marks the possible moon ingress identified by TK18.

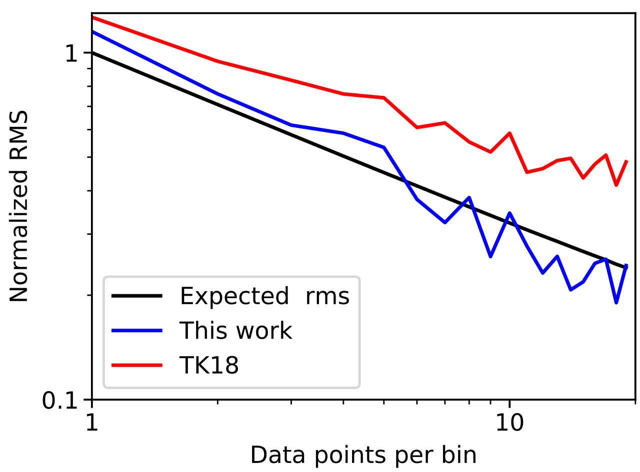

Figure 3. Light curve rms versus bin size for the best fit no-moon model. The fit to data from this work (blue line) agrees well with the expected photon-limited, $\sqrt{N}$ decrease in rms with bin size (black line). The TK18 rms (red line) ranges from $1.3-2\times$ the photon limit for bin sizes of 1 to 20 data points. The increase in relative rms for larger bin sizes indicates that time-correlated noise is present in the TK18 data.

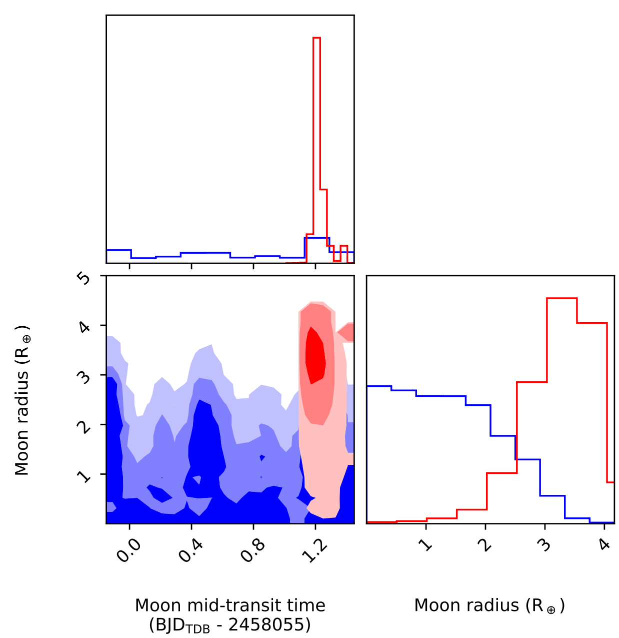

Figure 4. Posterior distributions

Peters, M. A., & Turner, E. L. 2013, ApJ, 769, 98, doi: 10.1088/0004-637X/769/2/98

Sengupta, S., & Marley, M. S. 2016, ApJ, 824, 76, doi: 10.3847/0004-637X/824/2/76

Simon, A. E., Szabó, G. M., Szatmáry, K., & Kiss, L. L. 2010, MNRAS, 406, 2038, doi: 10.1111/j.1365-2966.2010.16818.x

Skrutskie, M. F., Cutri, R. M., Stiening, R., et al. 2006, AJ, 131, 1163, doi: 10.1086/498708

Spake, J. J., Sing, D. K., Evans, T. M., et al. 2018, Nature, 557, 68, doi: 10.1038/s41586-018-0067-5

Stevenson, K. B., Désert, J.-M., Line, M. R., et al. 2014, Science, 346, 838, doi: 10.1126/science.1256758

Teachey, A., & Kipping, D. M. 2018, Science Advances, 4, eaav1784, doi: 10.1126/sciadv.aav1784

Teachey, A., Kipping, D. M., & Schmitt, A. R. 2018, AJ, 155, 36, doi: 10.3847/1538-3881/aa93f2

Van Der Walt, S., Colbert, S. C., & Varoquaux, G. 2011, Computing in Science & Engineering, 13, 22

Vanderburg, A., Rappaport, S. A., & Mayo, A. W. 2018, AJ, 156, 184, doi: 10.3847/1538-3881/aae0fc

Zhou, Y., Apai, D., Lew, B. W. P., & Schneider, G. 2017, AJ, 153, 243, doi: 10.3847/1538-3881/aa6481